

Investigation of three-dimensional grain-boundary structures in oxides through multiple-scattering analysis of spatially resolved electron-energy-loss spectra

N. D. Browning, H. O. Moltaji, and J. P. Buban

Department of Physics (M/C 273), University of Illinois at Chicago, 845 West Taylor Street, Chicago, Illinois 60607-7059

(Received 26 January 1998; revised manuscript received 2 April 1998)

Grain boundaries in oxide materials such as electroceramics, ferroelectrics, and high- T_c superconductors are known to dominate their overall bulk properties. The critical first step in a fundamental understanding of *how* they control the properties of the material is a determination of the atomic structure of the boundary. While this determination has traditionally been performed by transmission-electron microscopy, the images that are generated are only a two-dimensional projection of the atomic columns in the grain-boundary core. In addition, as the images are least sensitive to light elements, such as oxygen, the complete three-dimensional boundary structure is particularly difficult to determine. Employing electron-energy-loss spectroscopy in a scanning transmission-electron microscope, it is possible to obtain an oxygen K -edge spectrum that contains information on the three-dimensional electronic structure of the boundary. Using the multiple-scattering methodology, originally developed for x-ray absorption near-edge structure, this can be directly related to the local three-dimensional atomic structure. Contained in the spectrum is therefore all of the information needed to investigate the atomic scale structure-property relationships at grain boundaries. The application of the technique is demonstrated here for the 25° [001] symmetric tilt boundary in SrTiO_3 . [S0163-1829(98)03538-3]

I. INTRODUCTION

Oxide materials are currently being developed for such diverse electronic devices as varistors,¹ high- T_c superconductors,² and ferroelectrics.³ An intrinsic feature of all the oxides involved in these developments is the overwhelming tendency for defects to form during processing. Of the defects that can form, such as lattice vacancies, dislocations, stacking faults, second phases, and grain boundaries, it is grain boundaries that usually dominate the overall macroscopic performance of the material. The reason for this dominance is that grain boundaries inherently contain a concentration of defects far in excess of the equilibrium distribution in the bulk of the material.⁴ This excess of defects results in the boundary having a different atomic arrangement to the bulk and consequently, different properties. Hence, although grain boundaries are an atomic scale phenomenon and account for a small fraction of the material, they can have far reaching effects on the bulk scale properties and can control the technological application of the material.⁵

In light of the dominating influence of grain boundaries on the properties of oxides, it is not surprising that they are the subject of an intense research effort. As the properties of the boundary are known to be a function of the atomic structure, the usual approach to analyzing the structure-property relationships is through transmission-electron microscopy (TEM). Utilizing phase contrast imaging in TEM (Refs. 6 and 7) or Z -contrast imaging in scanning transmission-electron microscopy (STEM),⁸ the atomic structure of the boundary can be determined. However, the inherent limitation to both of these techniques is that an image simply provides a two-dimensional projection of the crystal structure. For phase contrast imaging, the determination of the three-dimensional structure involves simulating the image for a variety of test structures and accepting the best fit to the

image. Such a determination method therefore does not necessarily produce a unique solution for the boundary structure, as there is no way of knowing if the actual structure is included in the initial set of test structures. This is obviously not the optimum method to approach the analysis of unknown boundary structures.

The alternative to phase contrast imaging is Z -contrast imaging in the STEM. Although the Z -contrast technique generates an image that is essentially incoherent in nature,^{9,10} thereby avoiding much of the simulation needed for phase contrast imaging, direct interpretation of image intensity in the region of defects can be difficult (due to strain effects). Hence, to obtain the full three-dimensional atomic structure at the boundary, simulations are still required. Additionally, there is no information present in either of the imaging techniques concerning changes in chemical composition or electronic structure in the boundary core (the Z -contrast image may indicate a change in composition through an intensity change, but the chemical species cannot be identified). Subtle changes in composition and electronic structure that may have a strong impact on the structure-property relationships cannot be uniquely identified by an image and are therefore impossible to consider in theoretical calculations, as the number of possible permutations for a given boundary make computation times excessive. To be able to fully understand the effect of a grain boundary it is therefore imperative to increase the experimental data from the boundary.

Electron-energy-loss spectroscopy (EELS) is a technique that allows atomic scale fluctuations in composition and local electronic structure to be accurately quantified.¹¹ When performed in conjunction with Z -contrast imaging in the STEM it is possible to obtain these spectra with atomic spatial resolution.¹² Using the image as a map, spectra can be obtained from specified locations in the boundary plane. The

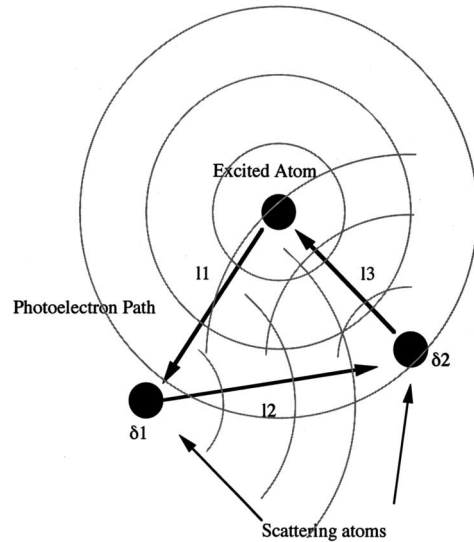
total amount of experimental information that is now available is therefore increased to include a two-dimensional projection of the atomic structure (from the image), an atomic resolution map of composition fluctuations that can be correlated with a location in the image (from the intensity of characteristic core-loss edges), and an atomic resolution measurement of the electronic structure that can also be correlated with a location in the image (from the fine structure of the core edges).

One methodology for combining all of this experimental information into a single structural model is through multiple-scattering analysis¹³ of the energy-loss spectrum. Although multiple-scattering theory was originally developed for the analysis of x-ray absorption spectra, its application to EELS is straightforward^{14,15} (only the method of excitation has changed from an x ray to an electron). Multiple-scattering calculations model the density of unoccupied states by considering the scattering of the photoelectron created during the excitation process, from neighboring atoms. The many paths that may be taken by a photoelectron alter the matrix elements for a particular transition due to constructive or destructive interference that occurs between the outgoing and returning photoelectron wave (Fig. 1). In effect, the resultant energy-loss spectrum may be described as a simple absorption edge of hydrogenic form, due to an isolated atom, with intensity modulations due to the atomic structure of the solid (Fig. 1), i.e., the absorption $\alpha(E)$ is given by

$$\alpha(E) = \alpha_0(E) \left[1 + \sum_{n=2} X_n(E) \right], \quad (1)$$

where $\alpha_0(E)$ is the atomic absorption and $X_n(E)$ is the multiple-scattering signal of order n ($n > 1$) that contains all the structural information.¹⁶ Since this description of the unoccupied density of states is based on a real space cluster of atoms, several unique opportunities are presented in this analysis. A lack of symmetry does not seriously affect the calculation, making it ideal for the study of low-symmetry defects, such as grain boundaries. The effects of dopant atoms may be simply investigated by substituting atom types within the cluster and recalculating the scattering. Multiple-scattering therefore allows spectral changes to be directly interpreted in terms of structural changes. As we have a starting structural model for grain boundaries in the Z-contrast image, with this analysis we can incorporate the third dimension and the compositional information by simulating the observed experimental energy-loss spectrum.

In this paper we discuss the application of this technique to determine the three-dimensional atomic structure of a 25° [001] symmetric tilt grain boundary in SrTiO₃. The choice of SrTiO₃ for this initial analysis was made for practical reasons (bicrystals of SrTiO₃ containing a single grain boundary can be purchased), and because it represents an “ideal” perovskite structure. Many of the oxide materials being developed for the applications listed above are based on perovskites. Hence, this framework to determine the three-dimensional grain-boundary structure and interpret the structure-property relationships on the atomic scale should be equally applicable to the high- T_c and ferroelectric materials.



$$L = 11 + \exp(i\delta 1) + 12 + \exp(i\delta 2) + 13$$

Constructive interference occurs for $L = n\lambda$

(a) Destructive interference occurs for $L = (n+1/2)\lambda$

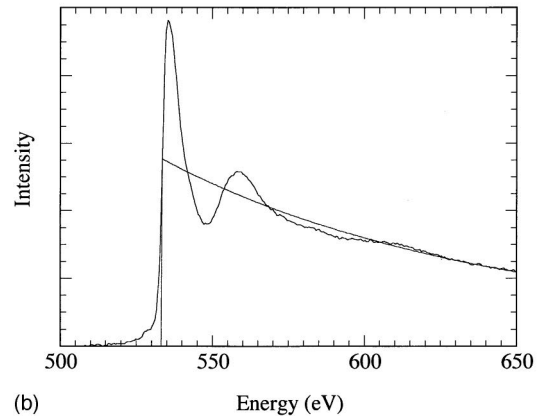


FIG. 1. (a) Multiple-scattering calculations model the density of unoccupied states by considering the scattering of the excited photoelectron from neighboring atoms. The resultant energy-loss spectrum may be described as a simple absorption edge of hydrogenic form, due to an isolated atom, with intensity modulations due to the atomic structure of the solid (b).

II. EXPERIMENTAL RESULTS

The experimental results presented here were obtained on the VG HB501 UX dedicated STEM at Oak Ridge National Laboratory. This instrument operates at an accelerating potential of 100 kV and has an optimum spot size (probe diameter) of 0.22 nm full width at half maximum (FWHM) on the surface of the specimen. Images are formed by scanning the probe over the specimen and displaying the integrated intensity of electrons scattered into the various detectors on a TV screen scanning at the same rate (Fig. 2). The Z-contrast imaging method makes use of the electrons scattered to high angles (75–150 mrad).⁸ By collecting the high-angle scattering over a large angular range, the major transverse coherent effects in the image are removed and the image can be considered as a simple convolution between the probe intensity profile and a specimen object function^{9,10} (Fig. 2). For scattering to high angles, the object function is localized at the atom cores (~ 0.01 nm) and the scattering intensity approxi-

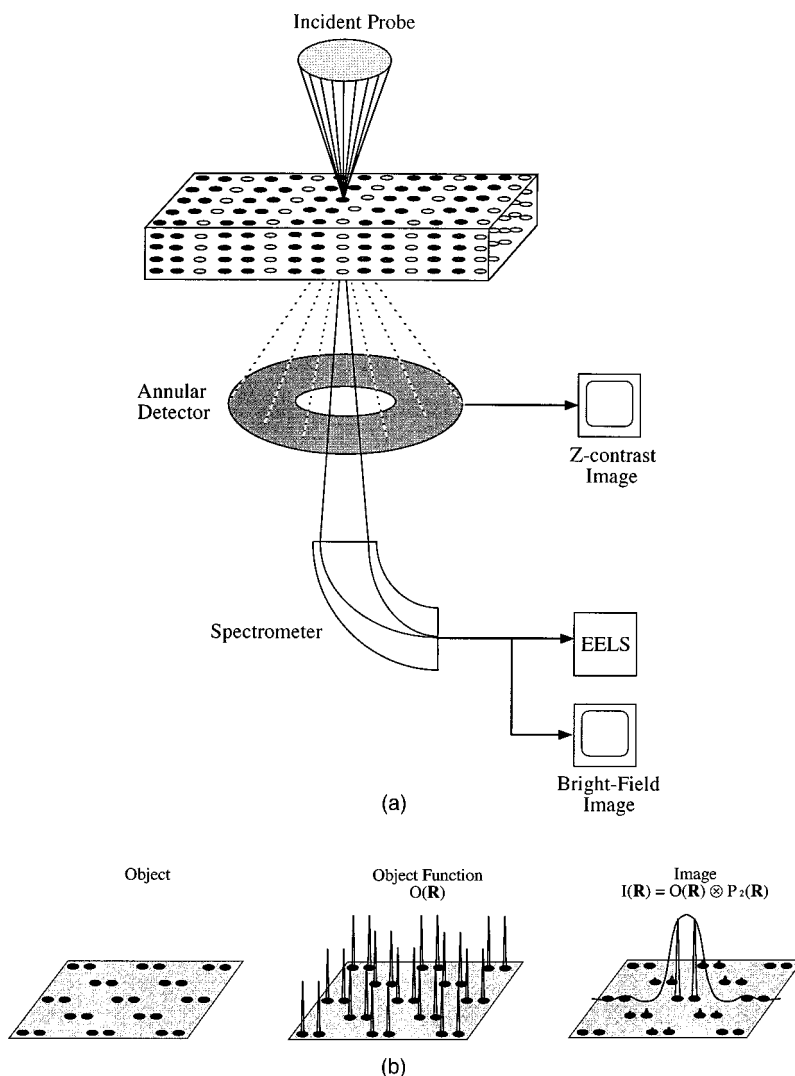


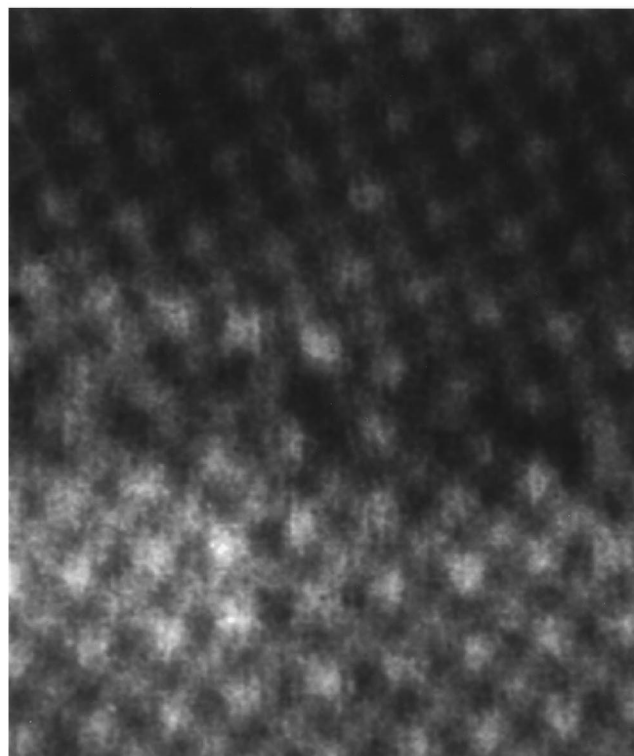
FIG. 2. (a) Schematic of the operation of the scanning transmission-electron microscope (STEM). (b) The Z-contrast image and electron-energy-loss spectrum can be considered to be a convolution of the probe intensity profile with an object function that represents the scattering cross section into the detector.

mates to the Z^2 dependence of the Rutherford scattering cross section. For crystalline materials in zone-axis orientations, if the probe size is smaller than the atomic column spacing, atomic columns can be illuminated individually and an atomic resolution map of the specimen generated.

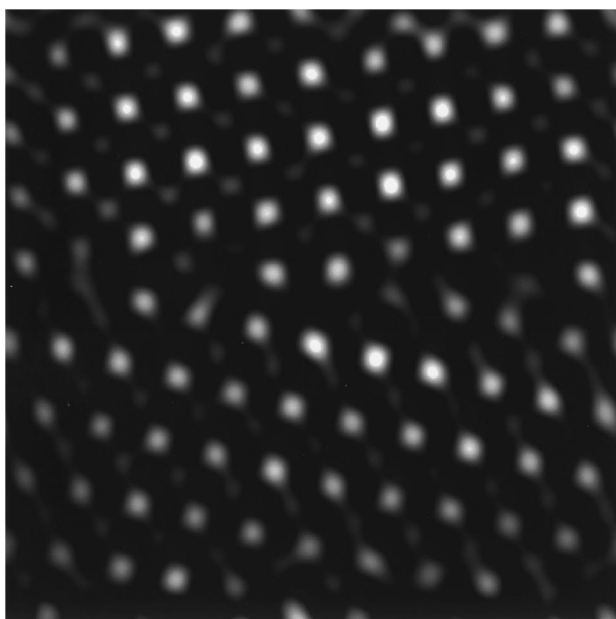
This result also holds for thicker specimens, where dynamical diffraction is manifested as a columnar channeling effect, thus preserving the spatial resolution and the “Z” contrast in the image.^{11,12} However, it must be noted that there are residual coherent effects within the atomic columns that can slightly modify the intensity of the image. These effects become pronounced at grain boundaries where strain effects can result in the boundary appearing either bright or dark. In the analysis described in this paper, no attempt is made to interpret the intensity in the Z-contrast image from atom columns at the boundary. The Z-contrast image is simply used as a structural image to determine the position of the probe during acquisition of the energy-loss spectrum. The initial boundary structural model is determined by applying crystal chemistry principles to this structural image (see later). A raw and Fourier filtered Z-contrast image of the 25° [001] tilt grain boundary in SrTiO_3 is shown in Fig. 3.

Fourier filtering is used here to remove high-frequency noise and enable the boundary structure to be viewed more easily.

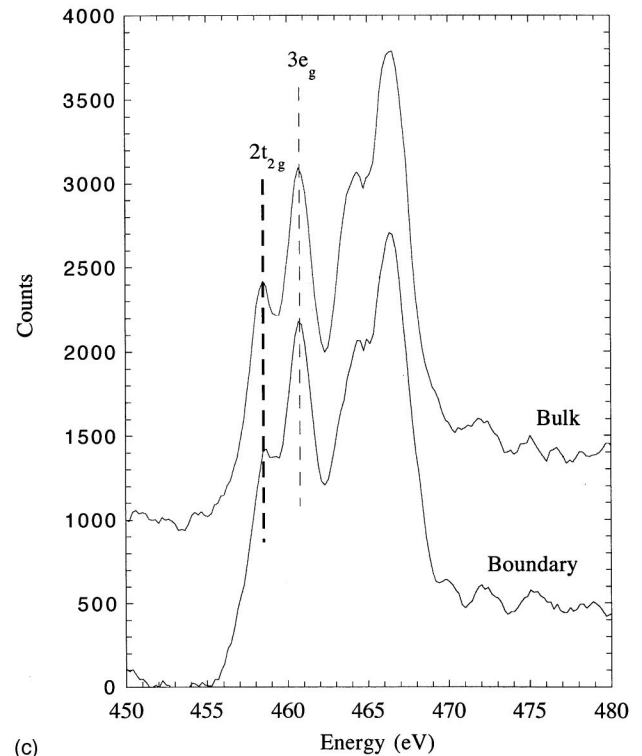
As can be seen from Fig. 2, the Z-contrast image does not interfere with the low-angle scattering that can be used for EELS. Therefore, using the image as a map, the probe can be stopped in defined locations in the structure for acquisition of spectra.^{12,17} In the case of the SrTiO_3 boundary analyzed here, concerns over electron beam induced damage caused the experiment to be performed in a slightly different manner. With the probe scanning continuously in a line parallel to the grain boundary (~ 4 nm in length), this line is stepped in single unit-cell intervals across the boundary. The spectra obtained therefore have single unit-cell resolution perpendicular to the boundary plane, but contain the integrated electronic structure parallel to the boundary plane. This acquisition method avoids potential problems in interpreting the spectra due to beam damage (to ensure that interpretation was not subject to damage, two spectra were acquired in each position and compared). While not generating a result representing the optimum in spatial resolution, this method does not affect the analysis of the three-dimensional structure of the grain-boundary plane (see later).



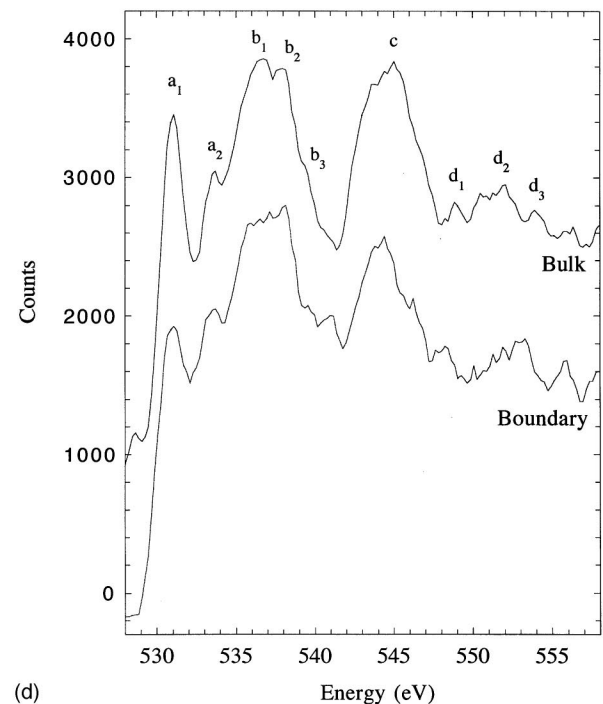
(a)



(b)



(c)



(d)

FIG. 3. (a) Raw Z-contrast image and (b) Fourier filtered image of the 25° [001] symmetric tilt grain boundary in SrTiO_3 . (c) Titanium $L_{2,3}$ -edge spectra from the bulk and the boundary plane. (d) Oxygen K -edge spectra from the bulk and the boundary plane. The feature at 529 eV in the oxygen K -edge spectrum from the bulk is afterglow in the CCD and not a real feature.

The spectrometer used for the EELS analysis is based on the magnetic prism design.¹¹ The dispersion at the exit slit of the spectrometer is enhanced by two quadrupoles and projected onto a yttrium aluminum garnet scintillator that is optically coupled to a charge-coupled device (Ref. 18) (Fig. 2). This approach allows single electron sensitivity to be at-

tained in the spectrum acquisition.¹⁹ This sensitivity is an essential part of the experiment as, although the current density in the probe is high enough to cause beam induced damage, the overall current is low (~ 10 pA). Hence, with this detection system, problems with counting statistics and specimen drift can be overcome with ~ 5 s integration times

TABLE I. Ratio integrated intensities in the main features of the experimental oxygen K -edge spectra from the bulk and grain boundary.

	Peak								
	a_1	a_2	b_1	b_2	b_3	c	d_1	d_2	d_3
Ratio (GB/bulk)	0.85 ± 0.03	1.02 ± 0.04	0.94 ± 0.04	0.96 ± 0.04	0.96 ± 0.03	0.92 ± 0.05	1.03 ± 0.06	0.95 ± 0.05	1.01 ± 0.05

for each spectrum. The resolution of the spectra obtained with this system is ~ 0.8 eV for core losses. Although this resolution is much poorer than the expected 0.2 eV energy spread of the cold field emission source, it is sufficient for analysis of the near-edge structure. The reason for the degradation of resolution is that large apertures are used in this analysis. Large apertures increase the signal levels and also ensure that the measured spectra are free from errors induced from diffraction effects and possible coherence effects in the energy loss event.²⁰

The two edges accessible in the study of SrTiO₃ are the titanium $L_{2,3}$ edge and the oxygen K edge. Spectra obtained from the bulk material and the boundary plane are shown in Fig. 3. Although spectra were obtained in unit cell steps across the boundary, for the analysis of the three-dimensional structure of the boundary plane we only need to know by how much the boundary spectrum changes relative to the bulk spectrum. In this regard, Table I shows the ratio between the intensities of main features in the oxygen K -edge spectrum in the bulk and at the boundary. The intensities of the peaks are determined by fitting Gaussian functions to each peak. Gaussian functions are chosen to model the intensities as the large apertures used in the experiment result in a broadening of the spectral features from the expected Lorentzian shape. Figure 4 shows the comparison between the experimental spectra and the Gaussians used to model the features. It can be seen that there are significant changes in the intensities of some of the peaks at the boundary. In addition to the result from the oxygen K edge, it can be seen that the titanium $L_{2,3}$ edge changes very little at the boundary with respect to the bulk with the onset, total intensity, and branching ratio being essentially unchanged (Fig. 3). However, it can be seen that there is a slight decrease in the peak labeled $2t_{2g}$. These peaks result from a crystal-field splitting and indicate a change in the symmetry of the Ti-O environment at the boundary.

III. DISCUSSION OF RESULTS

A. Development of a structural model for the boundary

The aim of the analysis described in this paper is to develop a means of determining the complete three-dimensional structure of a grain boundary without having to resort to complex theoretical calculations. Hence, what is required in the initial stages is a simple means of verifying that the number of atoms and approximate structure of the boundary is correct. One means to do this is through combined distance least-squares and bond-valence sum analysis of the Z -contrast image. This distance-valence least-squares analysis (DVLS) is based on a concept that was originally proposed by Pauling.²¹ In Pauling's rules for crystal chemistry, it is assumed that the formal valence state of a given atom is composed of contributions from all the nearest

neighbors. Additionally, the contribution to the valence from each of the neighbors should be as uniform as possible, i.e., the contributions to the formal valence state of an atom are shared equally between the nearest neighbors. These ideas have been further developed by Altermatt and Brown.^{22,23} In a systematic study of crystal structures they find that the contribution of a single bond to the formal valence state of the atoms involved follows the empirical relationship

$$S = \exp[(r_{ij} - r_0)/B], \quad (2)$$

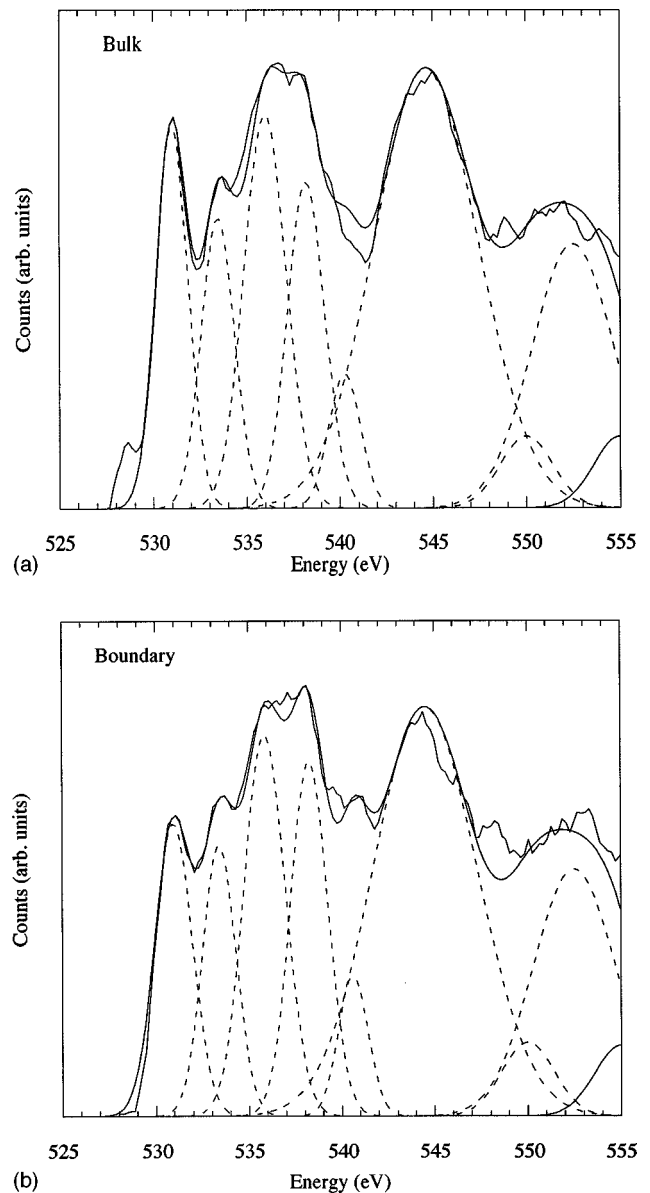


FIG. 4. Comparison of the experimental spectra from the bulk (a) and boundary (b) with the sum of the Gaussian functions used to estimate the intensities of each peak.

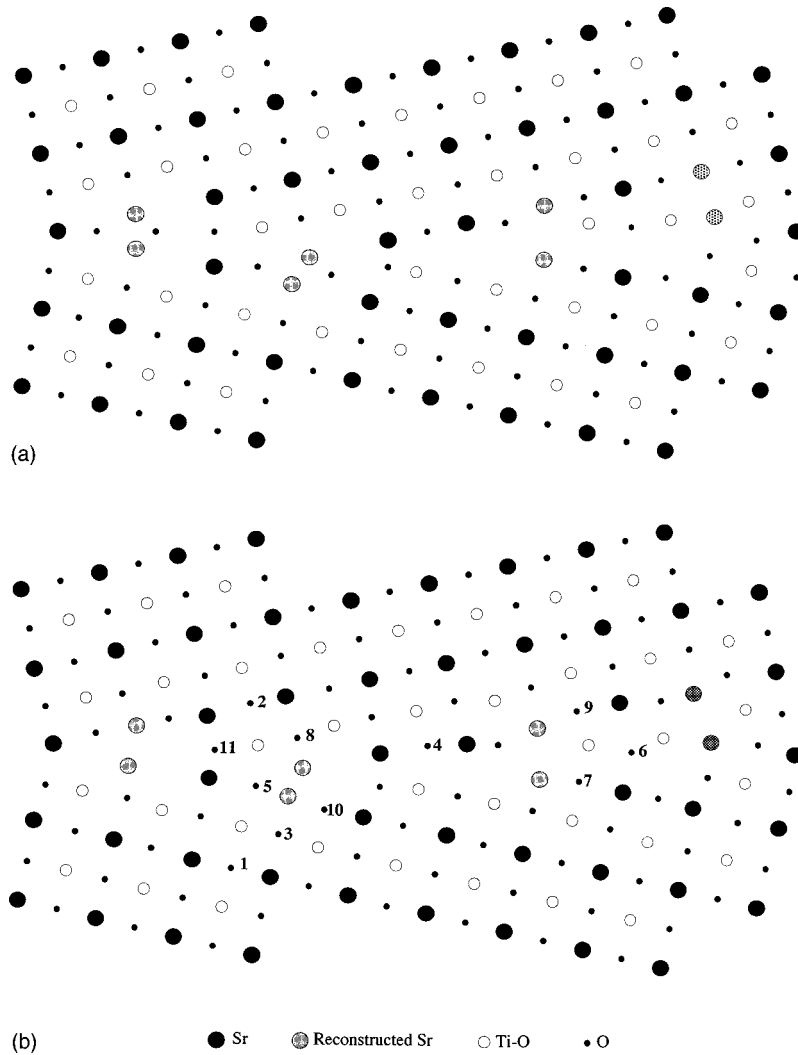


FIG. 5. (a) Schematic of the boundary structure determined from the Z-contrast image. (b) DVLS minimized structure.

where r_{ij} is the bond-length, r_0 is an equilibrium value for each atom pair, and B is a constant ($=0.37$). While this relationship is determined only for perfect crystal structures, there is every reason to believe that the same basic principles will apply for grain boundaries. (We know that the structure exists as we have an image, and if the same elements are involved it is reasonable to assume their bonding will be similar.) It is therefore possible to utilize this very simple pair potential between two atoms to check if the atoms in a proposed boundary structure are in a reasonable environment.²⁴ If the valence is too high, the bond length is too short and vice versa. Furthermore, the equilibration of the bonds to the nearest neighbors using the distance least-squares aspect of this formulation effectively forms a very basic energy minimization of the structure. Although such a minimization is by no means as accurate as *ab initio* calculations, a benefit of this simple approach is that it requires minimal computation capacity and within the errors ($\sim 10\%$), can verify that the number of atoms and their positions in the structure are physically reasonable.

Figure 5(a) shows the starting schematic of the 25° [001] tilt boundary shown in Fig. 3. The atom species are identified using the image intensities in the bulk of the grain (>2 nm from the boundary) and traced into the boundary core. This

analysis therefore does not interpret the intensities in the Z-contrast image from the boundary core and avoids problems associated with residual coherent effects in the image. Immediately obvious from the schematic are positions where two strontium columns appear too close together; like ion repulsion should preclude such a structure. However, we know that the Z-contrast detector does provide an incoherent transverse image and an atomic column must therefore exist in each of those positions. This problem can be overcome if these atomic columns are assumed to be reconstructed. A 2×1 reconstruction, i.e., each column is half occupied, avoids any problems with like ion repulsion and maintains the ion separation close to the bulk value. This 2×1 reconstruction has been shown to be valid by previous multiple scattering analysis²⁵ and the structure on which DVLS analysis is performed therefore includes these reconstructed atomic columns.

Figure 5(b) shows a schematic structure of the boundary after DVLS minimization. Once again, the aim in performing this minimization is to ensure that the atoms in the proposed structure have a reasonable electronic environment (valence) and that the forces on any one atom in the structure are not excessive. It therefore incorporates the fact that the experimental Z-contrast image is subject to errors in locating the

TABLE II. DVLS parameters before and after minimization of the structure in Fig. 4.

Element	No. of atoms	Valence Before minimization				Valence After minimization			
		High	Low	Average	Std. Dev.	High	Low	Average	Std. Dev.
Sr	54	3.04	1.08	2.09	0.296	2.19	1.79	2.05	0.088
Ti	38	6.14	3.48	4.06	0.528	4.32	3.75	4.04	0.126
O	129	5.19	0.72	2.03	0.390	2.33	1.79	2.03	0.093

positions of atoms (~ 0.02 nm) and that the oxygen positions are not known from the image. To perform the minimization, a formal valence state of the elements involved must be assumed. Oxygen (-2) and strontium ($+2$) are known to only exist in one formal valence state. The same is not true for titanium, where several valence states can exist ($+2$, $+3$, $+4$). However, we know from the titanium $L_{2,3}$ -edge spectrum at the boundary that there is very little change in the titanium $L_{2,3}$ -edge spectrum. Changes in valence state should be manifested as a change in the edge onset, integrated edge intensity, and branching ratio. Additionally, as the fine structure of the oxygen K edge is not radically changed, the coordination should also be extensively the same as the bulk. Therefore, in the minimization it is assumed that titanium at the boundary is in the same $+4$ formal valence state as the titanium in the bulk. Table II shows the bond-valence parameters before and after the minimization of the structure takes place. The resulting structure (and for that matter the starting structure) is essentially charge neutral, making it possible to now go on to use more sophisticated simulation codes if desired. However, we are now in a position where we can use the three-dimensional structure from any position in the boundary as a starting model to simulate the energy-loss spectrum with multiple-scattering analysis.

B. Analysis of the bulk spectrum

To understand the effect that the boundary atomic structure has on the electronic structure and therefore the energy-loss spectrum, it is first necessary to understand the fine structure of the oxygen K -edge spectrum obtained from bulk SrTiO_3 . In this paper, the multiple-scattering analysis is performed using the FEFF7 codes.¹³ These codes use the overlapping-atom prescription of Mattheiss²⁶ to model the atomic potential within the muffin-tin approximation. From the resulting potential, scattering phase shifts and matrix elements are calculated. Core hole effects are included using the $(Z+1)^*$ approximation¹⁵ where $*$ denotes the excited atom. For the purposes of these calculations, the atomic clusters are divided into shells of atoms where a single shell is composed of atoms that lie between two radii about the excited site. For the spectra presented here, the calculations were found to converge when the clusters include all atoms up to the eighth shell (6.173 Å from the excited atom). In these calculations, the order of scattering included in the spectra is controlled simply by placing an upper limit on the number of scattering events that are allowed. Figure 6 shows the simulation for the oxygen K -edge from bulk SrTiO_3 obtained using a cluster up to the eighth shell and including all orders of scattering. A comparison of the theoretical calcu-

lation and the experimental bulk spectrum is also shown. Here, a 1 eV broadening is added to the theoretical calculation to allow direct comparison with the experimental data.

In analyzing the oxygen K -edge, it is convenient to break the spectrum up into two sections. The first section, involving the first 5 – 10 eV above the threshold, has been previously identified as resulting from hybridization between the oxygen $2p$ and transition-metal (Ti) $3d$ levels.^{27,28} As described by de Groot *et al.*,²⁹ the perovskite structure represents the prototype for a tight-binding description of the TiO_6^{8-} cluster. Here, the crystal-field splitting results in $2t_{2g}$ states that are essentially pure π bonding and $3e_g$ states that are pure σ bonding (these features are mirrored in the titanium $L_{2,3}$ -edge spectrum). The stronger σ interaction increases the dispersion of the e_g band with the net result, which is reproduced in the experimental spectrum, being that the t_{2g} band (peak a_1) appears more intense and narrower than the e_g band (peak a_2). In the theoretical spectrum, the intensity and shape of peak a_1 is well reproduced, but peak a_2 is absent. The reason for its absence is rooted in the multiple-scattering method used to simulate the spectrum. The muffin-tin potentials are spherically symmetric and

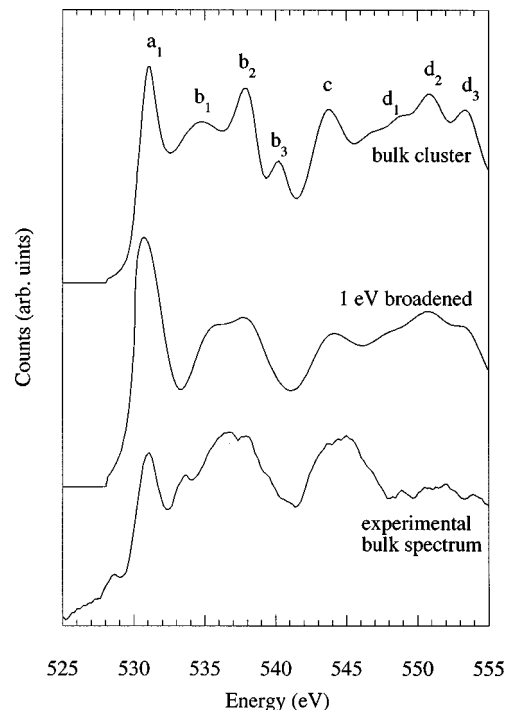


FIG. 6. Multiple scattering simulation of the oxygen K -edge spectrum from bulk SrTiO_3 . The simulation is broadened by 1 eV for comparison with the experimental spectrum.

TABLE III. The cluster compositions of the distinct oxygen atoms in the boundary plane compared to the bulk cluster.

Cluster	1	2	3	4	5	6	7	8	9	10	11	Average cluster	Full Cluster
Degeneracy	$x1$	$x2$	$x6$	$x1$	$x2$	$x1$	$x1$	$x3$	$x1$	$x2$	$x1$		
Shell 1	2 Ti	2 Ti	2 Ti	2 Ti	2 Ti	2 Ti	2 Ti	2 Ti	2 Ti	1 Ti	1 Ti	1.90 Ti	2 Ti
Shell 2	4 Sr	4 Sr	4 Sr	4 Sr	4 Sr	4 Sr	4 Sr	4 Sr	4 Sr	4 Sr	4 Sr	4.00 Sr	4 Sr
	8 O	8 O	3 O	8 O	8 O	8 O	8 O	7 O	7 O	6 O	6 O	7.52 O	8 O
Shell 3	6 O	6 O	5 O	5 O	5 O	5 O	4 O	6 O	6 O	5 O	6 O	5.33 O	6 O
Shell 4	8 Ti	7 Ti	8 Ti	7 Ti	7 Ti	8 Ti	7 Ti	7 Ti	8 Ti	7 Ti	7 Ti	7.43 Ti	8 Ti
Shell 5	8 Sr	8 Sr	8 Sr	8 Sr	8 Sr	6 Sr	6 Sr	8 Sr	6 Sr	8 Sr	8 Sr	7.71 Sr	8 Sr
	15 O	14 O	15 O	14 O	13 O	14 O	14 O	14 O	16 O	16 O	14 O	14.57 O	16 O
Shell 6	12 O	12 O	11 O	12 O	12 O	12 O	12 O	12 O	12 O	12 O	9 O	11.57 O	12 O
Shell 7	10 Ti	10 Ti	10 Ti	10 Ti	9 Ti	10 Ti	7 Ti	9.76 Ti	10 Ti				
Shell 8	8 Sr	8 Sr	8 Sr	8 Sr	8 Sr	8 Sr	7 Sr	8 Sr	8 Sr	8 Sr	8 Sr	7.96 Sr	8 Sr
	15 O	16 O	16 O	16 O	16 O	16 O	15 O	16 O	15 O	16 O	16 O	15.8 O	16 O

therefore do not include the d symmetry of the interaction between the oxygen $2p$ and titanium $3d$ orbitals and are not self-consistent (it may be that the lack of self-consistency is the dominating effect here, as the crystal-field splitting has been reproduced in rutile using muffin-tin potentials in a self-consistent Korringa-Kohn-Rostoker calculation³⁰). Although the crystal-field splitting may in some cases be reproduced by the second part of these simulations, the symmetry of the reflected photoelectron wave, this is not the case here. This may be due to the overlap of the peaks labeled b_1 , b_2 , and b_3 which mask the dispersed e_g (a_2) peak in the simulated spectrum. However, peak a_1 is accurately reproduced in the calculations and interpretation of the effect of the Ti nearest neighbors on the oxygen at the grain boundary will focus on the analysis of this peak.

The second part of the spectrum concerns the range 10–30 eV above threshold. In this regime, band structure calculations show that oxygen $2p$ states are hybridized with the weakly structured metallic $4sp$ band.²⁹ As such, the intensity modulations that occur in this energy range are not the result of transitions to bound states, but rather from interference effects resulting from multiple scattering of the excited photoelectron from neighboring atoms. As this is precisely the scattering that the FEFF7 codes are designed to calculate, it is not surprising that the theoretical spectrum reproduces these features accurately. It is also worthwhile restating that such multiple-scattering effects are very sensitive to the structure of the material. Hence, the scattering in this regime can give an accurate measure of changes in the atomic structure that occur at grain boundaries.

The backscattering of excited photoelectrons from various ions in transition metal oxides has been studied extensively.^{31–35} In particular, it has been found that O^{2-} ions are strong backscatterers and the main peaks in the spectrum can be assigned to resonance effects between the excited atom and the oxygen cages (shells) that surround it.³⁶ Although these ideas were primarily developed for binary transition-metal oxides, such as NiO, MnO, TiO₂, etc., the analysis is still applicable to SrTiO₃. However, in this case

the structure of the spectrum is modified by the more complicated composition of the material, i.e., more than one metal-oxygen interaction. Using the resonance argument,³⁶ the remaining main peaks in the oxygen k -edge spectrum can be assigned to the following interactions: peak b_2 results from intrashell scattering in the first shell of oxygen neighbors, peak c originates from single scattering from the shell containing the second-nearest oxygen neighbors, and peak d_2 originates from single scattering from the shell containing the first-nearest oxygen neighbors. The other peaks in the spectrum arise either from multiple-scattering events in higher shells (b_1 and d_1) or involve Sr atoms in the multiple-scattering path (b_3 and d_3).

C. Analysis of the boundary spectrum

With this analysis of the bulk spectrum in place, we are now in a position to interpret the spectral changes that occur at the grain boundary. In particular, peak a gives information on the coordination to the Ti nearest neighbors and peaks b_{1-3} , c , and d_{1-3} give an accurate and detailed analysis of the first and second-nearest oxygen neighbors. By comparing the experimental spectra from the bulk and boundary (Table I), the main changes occurring at the boundary seems to be decreases in peaks a_1 , b_1 , b_2 , c , and d_2 . A simple interpretation of this result suggests that atoms in the grain boundary plane have a reduced symmetry and reduced number of first- and second-nearest oxygen neighbors, i.e., a decrease in the backscattered intensity is caused simply by a decrease in the number of backscattering O^{2-} ions. We can investigate this concept further using atomic clusters for the oxygen atoms at the boundary determined from the model shown in Fig. 5(b).

In this structure 11 distinct oxygen sites can be identified [labeled in Fig. 5(b)]. The first eight coordination shells from these oxygen atoms and the first eight shells from the bulk structure are shown in Table III. It can be seen from these clusters that the oxygen atoms at the boundary have essentially the same environment as the oxygen atoms in the bulk except for the occasional atom missing from various shells

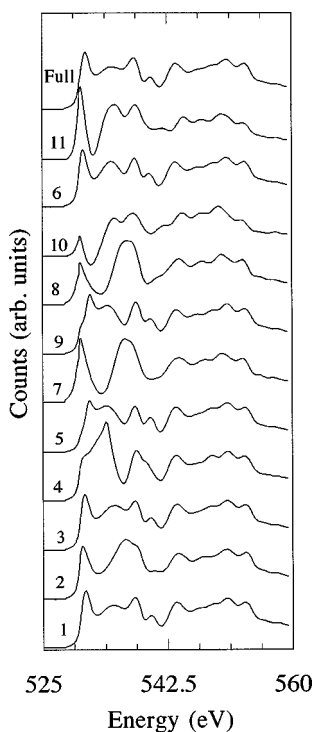


FIG. 7. Spectra obtained from the boundary clusters described in Table III from positions labeled in Fig. 4.

(this missing atom is an “effective” vacancy, i.e., it is the result of the misorientation angle and reconstruction of the boundary plane and is not a “real” lattice vacancy). It must be noted that there is some scatter in the position of the atoms in various shells is due to the fact that the DVLS minimization performed is not a complete energy minimization and only has a $\sim 10\%$ accuracy. However, this factor does not affect the analysis in great detail as the scatter in the atom positions simply broadens the spectral features (i.e., there is no longer a single defined distance for scattering paths from a given shell). To remove the effects of peak broadening, caused by a lack of energy minimization, the following simulations will use the atom positions from the bulk cluster with the number of atoms in each shell given by the clusters in Table III.

Figure 7 shows the multiple scattering calculations for the distinct oxygen atoms in the boundary core identified in Table III. Again the calculations were found to converge for a cluster up to the eighth shell and all orders of scattering were included in the calculations. The structures of the individual spectra are consistent with the interpretation used for the bulk spectrum concerning the origin of the spectral features. The experimental oxygen K -edge spectrum shown in Fig. 3 was acquired with the probe being continually scanned parallel to the boundary plane and therefore contains the integrated contributions from all of the oxygen sites listed in Table III. Figure 8 shows the multiple-scattering spectrum that results from summing all the contributions of the distinct oxygen sites in the boundary plane. Comparing this spectrum to the multiple-scattering simulation from the bulk, it can be seen that the experimental changes that are seen at the boundary are reproduced. These changes can be quantified in a similar manner to the experimental spectra by fitting Gaussians to the peaks. Table IV shows the relative intensities of

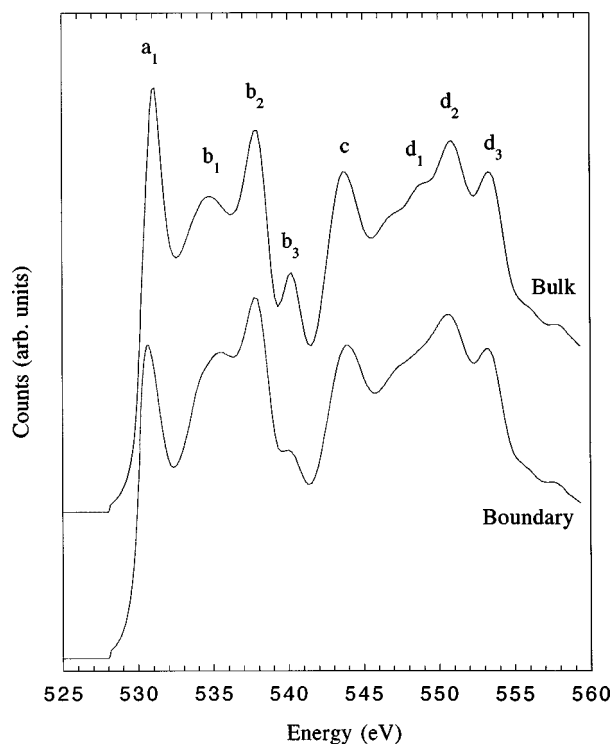


FIG. 8. Comparison of the simulated bulk spectrum with the integrated boundary spectrum.

the peaks in the two theoretical spectra compared to the experimental spectra. The result shows quantitative agreement with the experiment (there is some discrepancy in the peak labeled d_3 , but this peak is barely above the background noise in the experimental spectra and at the edge of the fitted energy range, and therefore expected to be subject to a large error) and indicates that the structure used for these simulations reproduces the observed near-edge structure at the boundary. It should be noted that improved statistics for peaks d would greatly enhance the accuracy in determining the grain-boundary structure by allowing the nearest-neighbor distance to be quantified in a similar manner to extended x-ray-absorption fine structure.³⁷

The multiple-scattering result determined above gives an extra degree of confidence in the three-dimensional structure of the boundary. The image itself is only a two-dimensional projection of the structure, and although we use crystal chemistry principles to create our model, the bond-valence potential is relatively inaccurate. Now, however, having reproduced the experimental changes in the spectra with our simulations, we can now more accurately identify the structural changes that occur at the grain boundary relative to the bulk. The decrease in peak a_1 is caused by the grain boundary distorting the linear Ti-O bonds in the bulk perovskite structure. The crystal-field splitting, peaks a_1 and a_2 , no longer represents the pure π^* and σ^* character as in the bulk, and results in the enhancement of peak a_2 with respect to peak a_1 (as seen experimentally). Although peak a_2 is not observed in the simulations, the decrease in peak a_1 is indicative of a distortion of the linear Ti-O chains in the structure and is quantitatively consistent with the experimental observations. This feature is also reproduced in the experimental titanium L -edge spectra. The decrease in peaks b_1 ,

TABLE IV. Ratio integrated intensities in the main features of the simulated oxygen K -edge spectra from the bulk and grain boundary. The experimental values are given in parentheses.

	Peak								
	a_1	a_2	b_1	b_2	b_3	c	d_1	d_2	d_3
Ratio MS (GB/bulk)	0.84		0.93	0.95	0.94	0.91	1.03	0.93	1.09
Ratio (GB/bulk)	0.85 ± 0.03	1.02 ± 0.04	0.94 ± 0.04	0.96 ± 0.04	0.96 ± 0.03	0.92 ± 0.05	1.03 ± 0.06	0.95 ± 0.05	1.01 ± 0.05

b_2 , c , and d_2 clearly represent a decrease in the number of oxygen backscatterers in each of the shells giving rise to the feature, i.e., the first- and second-nearest oxygen neighbors. This decrease in backscatterers is caused by the boundary misorientation and indicates that although the overall structure is charge neutral, there are local fluctuations in the number of atoms relative to the bulk, i.e., the “effective” vacancies mentioned earlier.

D. Structure-property relationships at the boundary

The atomic clusters around the oxygen atoms in the boundary now allow us to infer the structure-property relationships. Each of these clusters is missing atoms from various shells surrounding the central oxygen atom, which will lead to a local change in the charge distribution for this ionic material. However, before moving on to discuss the charge at the boundary and its effect on the properties, it is worthwhile to review the origin of these vacancies. In the previous section we defined the missing atoms as “effective” vacancies. (The term “effective” vacancy could equivalently be termed an “effective” reduction in coordination at the grain boundary. However, the individual clusters at the grain boundary indicate that the “effective” missing atoms do not occur in the same positions for the entire boundary plane and hence the term vacancy may be more appropriate.) The reason for this definition is that they are not atomic vacancies in the sense that the term is used in the bulk. For the bulk material, an atomic vacancy is defined as a lattice position that can and should be occupied by a particular atom type. In this case, all of the available lattice sites in the boundary are occupied. The “effective” vacancies arise because the boundary reconstruction and misorientation angle does not allow atoms to exist at certain positions. Hence, compared to an equivalent site in the bulk, the local environment of the atoms in the boundary plane is devoid of a certain number of atoms.

In the average boundary cluster shown in Table III, it can be seen that the reconstruction leads to strontium, titanium, and oxygen vacancies. While electrically, cation vacancies will compensate anion vacancies and vice versa, if we sum up the number of vacancies in the boundary cluster, there is a clear excess of oxygen vacancies in the boundary plane (the same effect is observed when considering clusters around Sr and Ti atoms in the boundary plane). This is consistent with the changes seen in the oxygen K -edge and titanium L -edge spectra obtained from the boundary and discussed in the previous sections. The observation of oxygen vacancies at the boundary may not be surprising as thermodynamics predicts that the surfaces of ionic materials should

contain an excess of positively charged cations.^{38–40} In these calculations, surfaces are considered to be perfect sinks and sources for vacancies, with the compositional variation arising from the difference in the energetics of forming a cation or anion vacancy. As a grain boundary forms when two surfaces meet, the reconstruction of the grain boundary into the lowest-energy configuration should therefore primarily involve the cations (the observation of partially occupied Sr columns in the Z -contrast image may be evidence for this). Continuing this argument further, this formation mechanism for grain boundaries should result in the boundary plane having a positive charge (as has been observed experimentally in I - V measurements¹ and electron holography⁴¹ performed on undoped SrTiO₃ grain boundaries). The observation here of oxygen vacancies in the boundary plane is certainly consistent with this idea. However, it should be noted that previous theoretical interpretation of the electrical properties of grain boundaries often considers them to be perfect sources and sinks for vacancies, although this is not always observed experimentally.⁴² This study indicates that the vacancies at the boundary are an intrinsic aspect of the reconstruction and misorientation angle. Hence, while we assume that the surfaces of the grains are perfect sources and sinks, the formation of the grain boundary by two surfaces meeting locks these vacancies in place.

In the commercially available SrTiO₃ bicrystals used in this study, both the bulk material and the grain boundaries were found to be practically insulators at room temperature.⁴³ This implies that the material is free from the presence of impurities that would dope the material either n -type or p -type depending on whether donor or acceptor impurities dominated (no trace of impurities were found either in the bulk or segregated to the boundary by EELS or energy dispersive x-ray spectroscopy). For such a material, where carriers induced by cation doping are negligible, the charge carrier concentration is dominated by oxygen vacancies and is obviously dependent on environmental conditions such as temperature and oxygen pressure (increasing temperature and decreasing oxygen pressure leads to an increase in the number of vacancies and therefore an increase in the number of charge carriers). Although each vacancy acts as a donor, contributing two electrons to the conduction band, the overall conduction mechanism is a mixture of electronic and ionic (through the motion of the oxygen ion vacancies). The results presented here are consistent with this idea for conduction except that the oxygen vacancies in the grain boundary plane are immobile. This means that, unless there are segregated acceptor cations at the boundary, the boundary plane will always be positively charged and act as a barrier

to the movement of oxygen ion vacancies (by reducing the number of sites for ion migration and an electrostatic repulsion of the positively charged vacancies) and a potential well for electrons (the positively charged barrier will lead to a negative space charge region).

Although this study has concentrated on undoped grain boundaries, commercial applications involving semiconducting oxides usually deliberately dope the material with either donor or acceptor ions to increase the conductivity.^{44–50} However, the same principle should always hold; the boundary charge is an intrinsic function of the atomic structure of the boundary (it is known from studies of metal-semiconductor interfaces that the formation of a Schottky barrier is a function of the interface structure⁵¹). Initial results suggest that acceptor doped (Mn^{3+}) boundaries have the same atomic structure as the undoped boundaries, with the acceptor ions simply replacing titanium in the boundary core.⁵² Using the boundary cluster in Table III, it can be seen that only a 10% substitution of Mn^{3+} is necessary to compensate for the excess of “effective” oxygen vacancies and cause the boundary to be negatively charged. Any increase above this level will quickly lead to a very large potential barrier (with a negatively charged boundary and positive space charge region) being formed at the boundary, as has been observed experimentally by electron holography.⁴⁰ Furthermore, the 0–90° angular range of [001] tilt boundaries in SrTiO_3 are known to be composed of only a few distinct structural units.⁵³ These structural units have essentially the same electronic configuration as the boundary shown here (as seen experimentally in energy-loss spectra), and therefore all [001] tilt boundaries should follow the same general rule.

IV. CONCLUSIONS

Multiple-scattering analysis of electron-energy-loss spectra is a powerful tool to analyze the structure of grain boundaries and defects. The information present in the spatially resolved energy-loss spectrum provides a level of characterization beyond conventional imaging techniques. This information can be correlated to provide detailed three-dimensional structure determinations from which the structure-property relationships at the boundary can be elucidated. By using this technique to investigate the 25° [001] symmetric tilt grain boundary in SrTiO_3 , it has been possible to quantify the number of “effective” oxygen, strontium, and titanium vacancies at the boundary induced through the misorientation angle and boundary reconstruction. There is found to be an excess concentration of oxygen vacancies that induces a net positive charge at the boundary. While this charge is small and has a minimal effect on the conductivity of the boundary relative to the bulk in the undoped material, the results highlight how preferentially segregating acceptor dopants at the boundary can greatly affect the electrical properties of the boundary. Such measurements indicate that the electronic properties of grain boundaries in oxide materials depend very sensitively on the composition and atomic structure of the boundary plane. These techniques are equally applicable to other oxide materials such as ferroelectrics and high- T_c superconductors, and may be used to help elucidate the structure-property relationships of defects in these materials on the atomic scale.

ACKNOWLEDGMENTS

We would like to thank Andreas Schroeder, Stephen Pennycook, and Gerd Duscher for stimulating discussions. This research is sponsored by the U.S. Department of Energy under Grant No. DE-FG02-96ER45610.

- ¹W. Heywang, *J. Am. Ceram. Soc.* **47**, 484 (1964).
- ²Q. Li, G. N. Riley, Jr., R. D. Parella, S. Fleshler, M. W. Rupich, W. L. Carter, J. O. Willis, J. Y. Coulter, J. F. Bingert, J. A. Parrell, and D. C. Larbelesstier, *IEEE Trans. Appl. Supercond.* **7**, 2026 (1997).
- ³See, for example, *Ferroelectric Thin Films II*, edited by A. I. Kingon, E. R. Myers, and B. Tuttle, MRS Symposia Proceedings No. 243 (Material Research Society, Pittsburgh, 1991).
- ⁴A. P. Sutton and R. W. Balluffi, *Interfaces in Crystalline Materials* (Oxford University Press, New York, 1995).
- ⁵D. Dimos, P. Chaudhari, and J. Mannhart, *Phys. Rev. B* **41**, 4038 (1990).
- ⁶K. L. Merkle and D. J. Smith, *Phys. Rev. Lett.* **59**, 2887 (1987).
- ⁷R. W. Fonda and D. E. Luzzi, *Philos. Mag. A* **68**, 1151 (1993).
- ⁸S. J. Pennycook and D. E. Jesson, *Phys. Rev. Lett.* **64**, 938 (1990).
- ⁹D. E. Jesson and S. J. Pennycook, *Proc. R. Soc. London, Ser. A* **441**, 261 (1993).
- ¹⁰D. E. Jesson and S. J. Pennycook, *Proc. R. Soc. London, Ser. A* **449**, 273 (1995).
- ¹¹R. F. Egerton, *Electron Energy Loss Spectroscopy in the Electron Microscope*, 2nd ed. (Plenum, New York, 1996).
- ¹²N. D. Browning, M. F. Chisholm, and S. J. Pennycook, *Nature (London)* **366**, 143 (1993).
- ¹³J. J. Rehr, R. C. Albers, and S. I. Zabinsky, *Phys. Rev. Lett.* **69**, 3397 (1992).
- ¹⁴R. Brydson, H. Sauer, W. Engel, J. M. Thomas, and E. Zeitler, *J. Chem. Soc. Chem. Commun.* **15**, 1010 (1989).
- ¹⁵R. Brydson, H. Sauer, and W. Engle, in *Transmission Electron Energy Loss Spectrometry in Materials Science*, edited by M. M. Disko, C. C. Ahn, and B. Fultz (The Minerals, Metals, and Materials Society, Warrendale, PA, 1992).
- ¹⁶A. Bianconi, J. Garcia, A. Marcelli, M. Benfatto, C. R. Natoli, and I. Davoli, *J. Phys. (Paris)* **46**, 39 (1985).
- ¹⁷P. E. Batson, *Nature (London)* **366**, 727 (1993).
- ¹⁸D. McMullan, J. M. Rodenburg, Y. Murooka, and A. J. McGibbon, *Inst. Phys. Conf. Ser.* **98**, 55 (1990).
- ¹⁹N. D. Browning and S. J. Pennycook, *Microbeam Anal.* **2**, 81 (1993).
- ²⁰S. J. Pennycook, D. E. Jesson, and N. D. Browning, *Nucl. Instrum. Methods Phys. Res. B* **96**, 575 (1995).
- ²¹L. Pauling, *J. Am. Ceram. Soc.* **51**, 1010 (1929).
- ²²D. Altermatt and I. D. Brown, *Acta Crystallogr., Sect. B: Struct. Sci.* **41**, 240 (1985).
- ²³I. D. Brown and D. Altermatt, *Acta Crystallogr., Sect. B: Struct. Sci.* **41**, 244 (1985).
- ²⁴M. M. McGibbon, N. D. Browning, M. F. Chisholm, A. J. McGibbon, S. J. Pennycook, V. Ravikumar, and V. P. Dravid, *Science* **266**, 102 (1994).

- ²⁵D. J. Wallis and N. D. Browning, *J. Am. Ceram. Soc.* **80**, 781 (1997).
- ²⁶L. Mattheiss, *Phys. Rev.* **133**, A1399 (1964).
- ²⁷L. A. Grunes, R. D. Leapman, C. N. Wilker, R. Hoffman, and A. B. Kunz, *Phys. Rev. B* **25**, 7157 (1982).
- ²⁸C. Colliex, T. Manoubi, and C. Ortiz, *Phys. Rev. B* **44**, 11 402 (1991).
- ²⁹F. M. F. de Groot, J. Faber, J. J. M. Michiels, M. T. Czyzyk, M. Abbate, and J. C. Fuggle, *Phys. Rev. B* **48**, 2074 (1993).
- ³⁰P. Rez, J. M. MacLaren, and D. K. Saldin, *Phys. Rev. B* **57**, 2621 (1998).
- ³¹A. Bianconi, M. Dell'Araccia, P. J. Durham, and J. B. Pendry, *Phys. Rev. B* **26**, 6502 (1982).
- ³²R. N. Sinha, P. Mahto, and A. R. Chetal, *Z. Phys. B* **81**, 229 (1990).
- ³³A. Bianconi, E. Fritsch, G. Galas, and J. Petiau, *Phys. Rev. B* **32**, 4292 (1985).
- ³⁴F. W. Lytle and R. B. Greggor, *Phys. Rev. B* **37**, 1550 (1988).
- ³⁵H. Kurata and C. Colliex, *Phys. Rev. B* **48**, 2102 (1993).
- ³⁶H. Kurata, E. Lefevre, C. Colliex, and R. Brydson, *Phys. Rev. B* **47**, 13 763 (1993).
- ³⁷J. C. H. Spence, *Ultramicroscopy* **18**, 165 (1985).
- ³⁸J. A. Kilner and R. J. Brook, *Solid State Ionics* **6**, 237 (1982).
- ³⁹J. Frenkel, *Kinetic Theory of Liquids* (Oxford University Press, New Jersey, 1946).
- ⁴⁰K. Lehovec, *J. Chem. Phys.* **21**, 1123 (1953).
- ⁴¹V. Ravikumar, R. P. Rodrigues, and V. P. Dravid, *J. Am. Ceram. Soc.* **80**, 1131 (1994).
- ⁴²W. D. Kingery, H. K. Bowen, and D. R. Uhlmann, *Introduction to Ceramics*, 2nd ed. (Wiley, New York, 1976).
- ⁴³V. P. Dravid (private communication).
- ⁴⁴Y.-M. Chiang and T. Takagi, *J. Am. Ceram. Soc.* **73**, 3278 (1990).
- ⁴⁵F. Noll, W. Münch, I. Denk, and J. Maier, *Solid State Ionics* **86-88**, 711 (1996).
- ⁴⁶M. Cherry, M. S. Islam, and C. R. A. Catlow, *J. Solid State Chem.* **118**, 125 (1995).
- ⁴⁷A. C. Redfield, *Phys. Rev.* **91**, 3397 (1953).
- ⁴⁸R. M. Waser, *J. Am. Ceram. Soc.* **72**, 235 (1989).
- ⁴⁹H. Ihrig, *J. Am. Ceram. Soc.* **64**, 619 (1981).
- ⁵⁰M. Vollman and R. M. Waser, *J. Am. Ceram. Soc.* **77**, 235 (1994).
- ⁵¹W. E. Spicer, I. Lindau, P. Skeath, C. U. Su, and P. W. Chye, *Phys. Rev. Lett.* **44**, 420 (1980).
- ⁵²G. Duscher, N. D. Browning, and S. J. Pennycook, *Phys. Status Solidi A* **166**, 327 (1998).
- ⁵³N. D. Browning and S. J. Pennycook, *J. Phys. D* **29**, 1779 (1996).